Int. J. Heat Mass Transfer. Vol. 35, No. 4, pp. 945–956, 1992
Printed in Great Britain

0017–9310/92 $5.00 + 0.00

Analysis of finite laminar opposed-jets with and without rigid-body rotation

S. S. HOU,† K. C. CHANG‡§ and T. H. LIN†

† Department of Mechanical Engineering, National Cheng-Kung University, Tainan, 70101, Taiwan, R.O.C.

‡ Institute of Aeronautics and Astronautics, National Cheng-Kung University, Tainan, 70101, Taiwan, R.O.C.

(*Received* 19 *October* 1990 *and in final form* 12 *March* 1991)

Abstract—The fluid mechanics and mixing process of steady, laminar, finite and opposed-jets are theoretically investigated. A finite-volume method is employed to numerically solve the corresponding transport equations. Calculated results are compared with the analytical similarity solutions and the experimental data for two cases of the non-identical opposed-jets, constituted by two different fluids, without rigid-body rotation and the identical opposed-jets with rigid-body rotation. Agreements show that the numerical solutions obtained from the complete transport equations yield accurate predictions, while the similarity solutions yield fair predictions under some limitations.

1. INTRODUCTION

FINITE opposed-jets with and without rigid-body rotation are of fundamental importance to understand local mixing phenomena in some combustible flows. In particular, the cases of opposed-jets with rigid-body rotation were used for simulating the flame interaction due to local vorticity [1–5]. For instance, Sohrab and co-workers investigated experimentally and theoretically the behaviors of the premixed flames [1, 2], the diffusion flames [3–5] and the transition of diffusion to premixed flames [6] in an opposed-jets flow (OJF) configuration when two cylindrical jets were separated with finite distance. These studies revealed the significant influences of flow vorticity on the flame behaviors, and disclosed a fact that the lack of complete knowledge concerning the fluid mechanics and mixing process of OJF restricted further understanding of these reacting flow problems. The theoretical study of the rotating and non-rotating OJFs thus becomes necessary.

In early analytical investigations, with objectives and basic equations closer to those of the present work, Batchelor [7] described general one- and two-parameter families of rotationally symmetric problems corresponding to the fluid motion bounded by two rigid disks of infinite diameter but either infinite or finite separation distance with arbitrary angular velocities. Only qualitative analysis of these flow problems is provided in this work. Proudman [8] as well as Seshadri and Williams [9] studied analytically the steady, laminar flows between two non-rotating porous disks of infinite diameter through which fluid was injected with the limit of large Reynolds number. Recently, Wang [10] investigated the impinging head-on jets of different fluid properties in the region near the stagnation point. The similarity solutions of the Navier–Stokes equations were obtained by matching all parameters at the interface. Goddard *et al.* [11] re-examined the steady flow problems bounded by two axisymmetric rotating disks of infinite diameter, which were the same as described in Batchelor's work [7], by solving the self-similar form of Navier–Stokes equations with the finite-difference method. As part of their work, an analytical solution for the special case of large Reynolds number boundary-layer limit was found by using the linearized theory. Recently, Lin [12] developed similarity solutions for the inviscid OJF when two identical jets undergo rigid-body rotation of equal angular speeds in the opposite directions. However, agreements between the similarity solutions and the experimental data were limited by the introduction of additional assumptions in the problem formulation.

Current significant progress of computational fluid dynamics and the advent of the high-speed computer have led to many numerical investigations in jet impingement problems such as the performance of Vertical-Takeoff-and-Landing (VTOL) aircraft in ground effect [13, 14] and in radial outward flow problems between two coaxial disks such as pumps, diffusers, rotating heat exchangers, disk brakes, etc. [15]. Very few numerical studies of complete transport equations related to the present work can be found in open literature. Huang and MacInnes [16] performed numerical simulation of the outwash flow arising from the collision of two identical jets using three different turbulence models.

The objective of this work is to numerically analyze the transport processes in the finite, opposed identical/non-identical jets bounded between two

§ Author to whom correspondence should be addressed.

NOMENCLATURE

A, B integration constant
d nozzle diameter [mm]
D molecular diffusivity [$m^2 s^{-1}$]
f function of x defined in equation (A1)
F, G, H functions of z defined in equation (A7)
Fr Froude number, $(u_2^0)^2/gL$
g gravity [$m s^{-2}$]
K constant
L separation distance between two disks [m]
M molecular weight
OJF opposed-jets flow
p pressure
r, x radial and axial coordinates, respectively
R universal constant
Re Reynolds number, $\rho_2^0 u_2^0 L/\mu_2^0$
RL radial width of computational domain
Ro Rossby number, $\omega L/u^0$
Sc Schmidt number, $\mu_2^0/\rho_2^0 D$
T temperature
u, v, w axial, radial and circumferential velocity components, respectively
x_i mole fraction of species i
XL axial length of computational domain
Y_i mass fraction of species i
z transformed axial coordinate.

Greek symbols
Λ coefficient defined in equation (4)
μ molecular viscosity
ρ density
ϕ dependent variable
Ψ stream function defined in equation (A1)
ω rotation speed [s^{-1}].

Superscripts
0 inlet position (dimensional form)
* dimensional form
′ differentiation.

Subscripts
i, j running indices for species
s stagnant position
1, 2 upper and lower parts of flowfield.

porous disks with or without rigid-body rotation. These calculated results are compared with the analytical similarity solutions and the experimental data obtained by Lin [12].

2. PROBLEM DESCRIPTION

The OJF system [1, 3, 12], schematically shown in Fig. 1(a), consists of two identically-aligned, cylindrical injection nozzles with 51 mm i.d. (d_i) and 53 mm o.d. (d_o), which can rotate about their axis of symmetry. Each injection nozzle is driven by a variable-speed motor which allows for independent control of angular velocity and rotation direction. A series of small wire-mesh screens and honeycombs are used to ensure rigid-body rotation of the gas inside the injection nozzles and to yield uniform velocity distributions at the exit planes of the injection nozzles. The exit planes of the injection nozzles can, therefore, be imagined as two porous disks. The separation distance (L) between these two exit planes is 22 mm. The lower injection nozzle is installed with an exhaust jacket for removal of the injecting fluids. The radial, axial and circumferential velocity components were measured using one-component laser Doppler velocimeter in the back-scattering mode. Magnesium oxide powder centered around 1 μm in size was used as the seedings for laser light scattering. Absolute magnitudes of velocities below about 0.05 $m s^{-1}$ cannot be precisely measured as a result of seeding mobilization difficulty and small signal to noise ratios. The measurements of the axial velocity component close to the stagnation plane as well as the measurements of the radial and circumferential velocity components near the axis of OJF may, therefore, be associated with significant errors. The qualitative aspects of the flow fields were performed by flow visualization obtained with laser-sheet-light illumination of magnesium oxide powder. Details of the experimental facility and procedure are referred to in ref. [12].

Three steady-state cases of OJF with finite separation distance: identical (air–air) and non-identical (He–air) OJFs without rigid-body rotation as well as identical OJF with rigid-body rotation are investigated. Calculations of the axisymmetrically rotating, mixing problems require the simultaneous solutions of the transport equations representing the conservation of species, mass, and momentum. The mass transport accounting for the inter-diffusion between He and air is modelled by Fick's law. The density of the gas mixture is given, according to the ideal gas equation, by

$$\rho = p/RT\left(\frac{Y_{He}}{M_{He}} + \frac{Y_{air}}{M_{air}}\right) \tag{1}$$

where

$$Y_{air} = 1 - Y_{He}. \tag{2}$$

For determination of the viscosity of the gas mixture, the semiempirical formula of Buddenberg and Wilke [17] is adequate and is expressed by

$$\mu = \sum_{i=1}^{2}\left(x_i\mu_i \Big/ \sum_{j=1}^{2} x_j\Lambda_{ij}\right) \tag{3}$$

in which

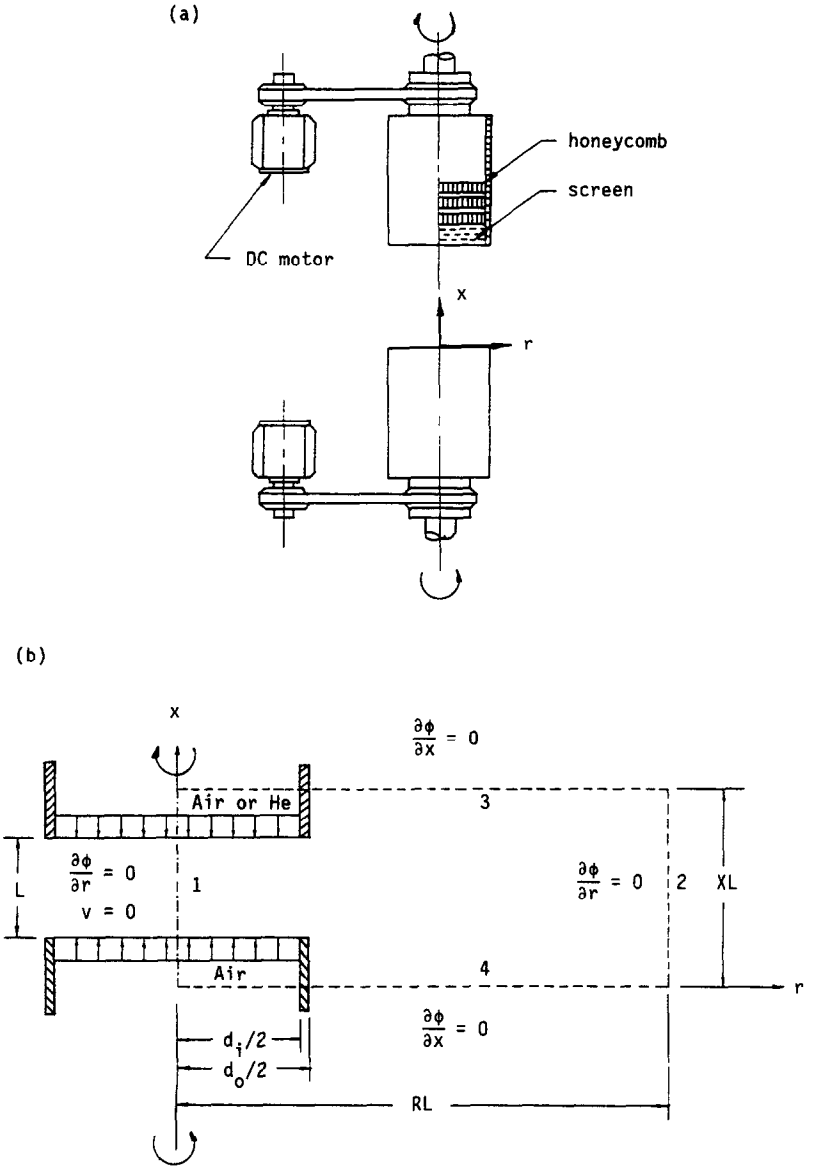

FIG. 1. Schematics of (a) the experimental setup and (b) the computational domain of the finite, opposed-jets flow.

$$\Lambda_{ij} = \left[1+\left(\frac{\mu_i}{\mu_j}\right)^{1/2}\left(\frac{M_j}{M_i}\right)^{1/2}\right]^2 \Big/ \left[8\left(1+\frac{M_i}{M_j}\right)\right]^{1/2}. \quad (4)$$

Here x_i is the mole fraction of species i which can be converted from the mass fraction as follows

$$x_i = Y_i \Big/ \sum_{j=1}^{2}\left(Y_j \frac{M_i}{M_j}\right). \quad (5)$$

The value of diffusivity D for the present binary (He and air) system is estimated to be 8.1×10^{-5} m^2 s^{-1} at 101.3 kPa and 298.2 K (room temperature with uncertainty of ± 2 K) by using the formula developed by Slattery and Bird [18]. The viscosities of air and He are 1.851×10^{-5} and 1.987×10^{-5} kg m^2 s^{-1}, respectively.

3. THEORETICAL ANALYSIS

Both analytical and numerical analyses are discussed in this section. It is noted that the numerical analysis allows us to investigate the real transport phenomena occurring in OJF without any simplification, while some approximations must be made for analytical analysis in order to obtain the self-similar solutions.

3.1. *Numerical analysis*

The transport equations of Table 1 are manipulated into a general partial differential form

$$\frac{\partial}{\partial x}\left(\rho u\phi - \Gamma_\phi \frac{\partial \phi}{\partial x}\right) + \frac{1}{r}\frac{\partial}{\partial r}\left(\rho v r\phi - \Gamma_\phi r \frac{\partial \phi}{\partial r}\right) = S_\phi \quad (6)$$

Table 1. Governing equations for rotating, mixing flow field

ϕ	Γ_ϕ	S_ϕ
1	0	0
u	$\frac{\mu}{Re}$	$-\frac{\partial p}{\partial z}+\frac{1}{r}\frac{\partial}{\partial r}\left(\frac{\mu}{Re}r\frac{\partial v}{\partial x}\right)+\frac{1}{3}\frac{\partial}{\partial x}\left(\frac{\mu}{Re}\frac{\partial u}{\partial x}\right)-\frac{2}{3}\frac{\partial}{\partial x}\left[\frac{\mu}{Re}\frac{1}{r}\frac{\partial}{\partial r}(rv)\right]+\frac{\rho_\infty-\rho}{Fr}$
v	$\frac{\mu}{Re}$	$-\frac{\partial p}{\partial r}-\frac{2\mu}{Re}\frac{u}{r^2}+\frac{\rho w^2}{r}+\frac{1}{r}\frac{\partial}{\partial r}\left(\frac{\mu}{Re}r\frac{\partial v}{\partial r}\right)+\frac{\partial}{\partial x}\left(\frac{\mu}{Re}\frac{\partial u}{\partial r}\right)-\frac{2}{3}\frac{\partial}{\partial r}\left(\frac{\mu}{Re}\frac{\partial u}{\partial x}\right)-\frac{2}{3}\frac{\partial}{\partial r}\left[\frac{\mu}{Re}\frac{1}{r}\frac{\partial}{\partial r}(rv)\right]$
w	$\frac{\mu}{Re}$	$-\frac{\rho vw}{r}-\frac{w}{r^2}\frac{\partial}{\partial r}\left(\frac{\mu}{Re}r\right)$
Y_{He}	$\frac{\rho}{Re\,Sc}$	0

$Re=\rho_2^0u_2^0L/\mu_2^0$, $Sc=\mu_2^0/\rho_2^0D$, $Fr=(u_2^0)^2/gL$.

that permits a single solution procedure to be used for calculation. The finite-volume method incorporated with the SIMPLER algorithm and the power-law scheme [19] is employed to obtain the numerical solution. The inactive regions inside the upper and lower nozzles (see Fig. 1(b)) are treated numerically by the blocking-off technique [19]. The blocking-off technique consists of establishing known values of the relevant ϕs (internal boundary conditions) in the inactive regions. Nevertheless, this technique is somewhat wasteful of computer efforts in comparison with the technique such as the body-fitted coordinate [20]. Notwithstanding this consideration, the convenience of using a regular grid layout offers a significant advantage.

Boundary conditions for the axis of symmetry, entrainment boundaries, inlet and outlet are required to be specified. For the symmetric axis denoted as plane 1 in Fig. 1(b), the assumption of gradient-type condition, $\partial\phi/\partial r=0$, is made except for the radial velocity component which is itself zero. For the upper and lower entrainment boundary (denoted as planes 3 and 4), the zero-gradient conditions are assumed, provided that XL is large enough. The outlet boundary condition (at plane 2) is assumed to be fully developed. Test predictions have been performed by extending the lengths of XL (66 mm) and YL (130 mm) longer than the present ones ($XL=44$ mm and $YL=110$ mm). The influences of the enlarged computational domain on the predictions are negligibly small. This implies that the assumed entrainment and outlet boundary conditions for the investigated geometry are acceptable. According to the experimental condition stated in Section 2, uniform distributions of axial velocity and zero radial velocity are specified at the two exit planes of the upper and lower nozzles. The distributions of circumferential velocity at these two planes are given by

$$w=2\pi r\omega L/u_1^0. \tag{7}$$

The mesh layout used for calculation consists of 52×80 non-uniformly distributed grid nodes for entire computational domain of (x,r), with a dense gridline concentration in the region between the two nozzles. Mesh refinement test (comparing to the result with the mesh of 72×100) reveals that this non-uniform mesh design has generated a nearly mesh-independent solution.

Iteration convergence refers to the attainment, to within some tolerance, of an acceptable solution to the equation which requires $\phi_{new}=\phi_{old}$. The convergence criterion adopted in the present calculation is that the maximum value of residual is less than 10^{-5} in the entire computational domain and for any of the dependent variables.

3.2. *Analytical analysis*

Consider an axisymmetric OJF as depicted in Fig. 1 but bounded by two cylindrical porous disks with infinite diameter. Only two special cases adopted from ref. [12] are illustrated in the following for comparison.

3.2.1. *Non-identical OJF without rigid-body rotation.* Further assumptions should be made to simplify the governing equations described in Table 1 so that the similarity solution can be found. The buoyancy effect and the dilatation effect (the volume change of a fluid element due to species mixing) are assumed to be negligible. As a matter of fact, the numerical solutions to the complete governing equations in Table 1 show that these two effects are, indeed, negligibly small for the investigated problem. These two assumptions are, thus, appropriate. The two fluids injecting through two porous disks are with density ρ_i and viscosity μ_i. Subscript $i=1$ and 2 represent the upper (He) and lower (air) flow fields,

respectively. These two fluids are assumed to be immiscible and to be separated by an interface (stagnant) plane [3, 4]. With this assumption, ρ_i and μ_i are constant in each flow region, and the momentum equations are, then, decoupled with the species continuity equation. The governing equations and their boundary conditions associated with the foregoing assumptions now become as follows:

$$\frac{1}{r}\frac{\partial}{\partial r}(rv_i)+\frac{\partial u_i}{\partial x}=0 \tag{8}$$

$$v_i\frac{\partial u_i}{\partial r}+u_i\frac{\partial u_i}{\partial x}=-\frac{\partial p}{\partial x}+\frac{1}{Re_i}\left[\frac{1}{r}\frac{\partial}{\partial r}\left(r\frac{\partial u_i}{\partial r}\right)+\frac{\partial^2 u_i}{\partial x^2}\right] \tag{9}$$

$$v_i\frac{\partial v_i}{\partial r}+u_i\frac{\partial v_i}{\partial x}=-\frac{\partial p}{\partial r}+\frac{1}{Re_i}\left[\frac{1}{r}\frac{\partial}{\partial r}\left(r\frac{\partial v_i}{\partial r}\right)+\frac{\partial^2 v_i}{\partial x^2}-\frac{v_i}{r^2}\right] \tag{10}$$

$$u_1(r,1)=-1 \quad \text{and} \quad v_1(r,1)=0 \tag{11a}$$

$$u_2(r,0)=1 \quad \text{and} \quad v_2(r,0)=0 \tag{11b}$$

$$u_1(r,x_s)=u_2(r,x_s)=0 \tag{11c}$$

$$\frac{\partial v_1}{\partial x}(r,x_s)=\frac{\partial v_2}{\partial x}(r,x_s)=0 \tag{11d}$$

where x_s denotes the axial position of the stagnant plane. The coordinates and velocity components are non-dimensionalized by the separation distance L and the magnitude of injection velocity, respectively. To simplify the problem, we let the injection velocities u_1^0 and u_2^0 satisfy $u_1^0=-u_2^0$.

Based upon the formulation shown in ref. [12] and the Appendix, the inviscid solutions were determined as

$$u_1=\left(\frac{1-x}{1-x_s}\right)^2-1 \tag{12}$$

$$v_1=\frac{1-x}{(1-x_s)^2}r \tag{13}$$

and

$$u_2=1-\left(\frac{x}{x_s}\right)^2 \tag{14}$$

$$v_2=\frac{x}{x_s^2}r \tag{15}$$

for the upper and lower parts of the flow field, respectively. The position of the stagnant plane can be determined by balancing the axial inertia of the upper and lower jets and is expressed as

$$x_s=\left\{1+\left|\frac{u_1^0}{u_2^0}\right|\left(\frac{\rho_1}{\rho_2}\right)^{1/2}\right\}^{-1}. \tag{16}$$

For a particular non-isothermal situation when the two molecular weights of the upper and lower jets are identical, the result in equation (16) can be rewritten in the form

$$x_s=\left\{1+\left|\frac{u_1^0}{u_2^0}\right|\left(\frac{T_2}{T_1}\right)^{1/2}\right\}^{-1} \tag{17}$$

which is the same as obtained by Seshadri and Williams [9].

For the viscous solution, equation (A4) is solved numerically using the Runge–Kutta method.

3.2.2. *Identical OJF with rigid-body rotation.* Two porous disks shown in Fig. 1 are made to rotate about the axis of symmetry in the opposite directions. The rigid-body rotating motion of the porous disk yields an initial constant angular speed ω to the injected fluid at the exit planes of the disk. To simplify the problem, an identical OJF is chosen for analysis and $x_s=0.5$. Due to the symmetric characteristic about the stagnant plane, only the lower half part of flow field $0<x<0.5$ is examined in the following. The governing equations and the required boundary conditions are specified as

$$\frac{1}{r}\frac{\partial}{\partial r}(rv)+\frac{\partial u}{\partial x}=0 \tag{18}$$

$$v\frac{\partial u}{\partial r}+u\frac{\partial u}{\partial x}=-\frac{\partial p}{\partial x}+\frac{1}{Re}\left[\frac{1}{r}\frac{\partial}{\partial r}\left(r\frac{\partial u}{\partial r}\right)+\frac{\partial^2 u}{\partial x^2}\right] \tag{19}$$

$$v\frac{\partial v}{\partial r}+u\frac{\partial v}{\partial x}-\frac{w^2}{r}=-\frac{\partial p}{\partial r}+\frac{1}{Re}\left[\frac{1}{r}\frac{\partial}{\partial r}\left(r\frac{\partial v}{\partial r}\right)+\frac{\partial^2 v}{\partial x^2}-\frac{v}{r^2}\right] \tag{20}$$

$$v\frac{\partial w}{\partial r}+u\frac{\partial w}{\partial x}+\frac{vw}{r}=\frac{1}{Re}\left[\frac{1}{r}\frac{\partial}{\partial r}\left(r\frac{\partial w}{\partial r}\right)+\frac{\partial^2 w}{\partial x^2}-\frac{w}{r^2}\right] \tag{21}$$

$$u(r,0)=1, \quad v(r,0)=0, \quad w(r,0)=2\pi r\,Ro \tag{22a}$$

$$u\left(r,\frac{1}{2}\right)=0, \quad \frac{\partial v}{\partial x}\left(r,\frac{1}{2}\right)=0, \quad w\left(r,\frac{1}{2}\right)=0 \tag{22b}$$

where the Rossby number Ro is defined by

$$Ro=\frac{\omega L}{u^0}. \tag{23}$$

The similarity solution is developed following von Kármán [21] by requiring that u, v/r and w/r are all functions of x alone. Following the detailed procedure shown in the Appendix, the velocity components can be found as

$$u=\frac{\cos 2z-\cos Ro}{1-\cos Ro} \tag{24}$$

$$v=Ro\,r\frac{\sin 2z}{1-\cos Ro} \tag{25}$$

$$w=Ro\,r\frac{\cos 2z-\cos Ro}{1-\cos Ro}. \tag{26}$$

The viscous solutions can be obtained by applying the Runge–Kutta numerical method to equations (A9)–

(A11) with the boundary conditions of equation (A13).

4. RESULTS AND DISCUSSION

Numerical predictions are presented together with the analytical similarity solutions and the experimental data coming from ref. [12].

4.1. *OJF without rigid-body rotation*

Two cases are investigated in this subsection. The first case is the identical (air–air) OJF with $-u_1^0 = u_2^0 = 0.453$ m s^{-1} and $Re = 660$. The second one is the non-identical (He–air) OJF in which the light fluid, He, is injected downward from the upper nozzle and the heavy fluid, air, is injected upward from the lower nozzle. The two initial velocities are the same as the case of the identical OJF but the ratio of initial momentum fluxes of He jet to air jet is equal to $M_{He}/M_{air} = 0.1382$.

Figure 2 presents the comparisons of the numerical and analytical predictions of centerline axial velocities for both identical and non-identical cases of OJF. Since the measurements of centerline axial velocity for the non-identical OJF are not available in ref. [12], only the experimental data for the identical OJF is included in Fig. 2. It is seen from the comparison of the theoretical and experimental results for the identical OJF that the numerical and both similarity (inviscid and viscous) solutions are in good agreement with the measurements. The presumption of infinitely large disk-diameters leads to slight discrepancies between the numerical and similarity solutions. Nevertheless, the discrepancies between the numerical and similarity solutions become relatively significant in the case of non-identical OJF as shown in Fig. 2. It just happens that the inviscid similarity solutions of the centerline axial velocity have smaller differences from the numerical solutions than the viscous similarity solutions for both identical and non-identical OJFs.

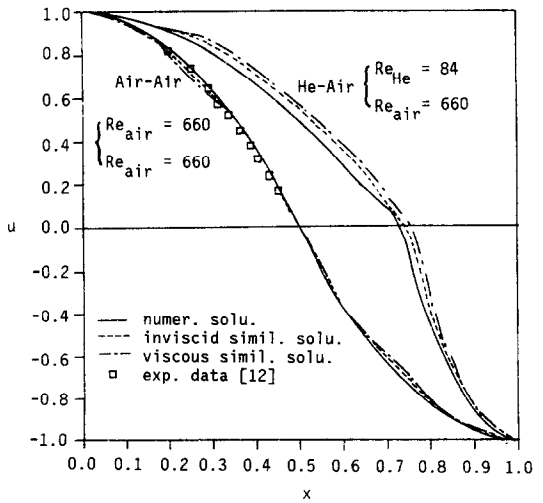

FIG. 2. Comparisons of numerical and similarity solutions of axial velocity with experimental data for identical and non-identical OJFs without rigid-body rotation at axis of symmetry.

The variations of radial velocity along the axial coordinate obtained either theoretically or experimentally at six radial sections for the identical OJF are presented in Fig. 3. It is found that the differences between the inviscid and viscous similarity solutions of radial velocity are still negligibly small, as discussed before. The viscous solutions are, therefore, not presented in Fig. 3. The comparison reveals that the inviscid similarity solutions incorporated with the presumption of infinitely large disk-diameters are consistent with the numerical solutions which are solved directly from the Navier–Stokes equations without approximation. The theoretical and experimental solutions shown in Fig. 3 are in good agreement except in the region close to the stagnant plane. These inconsistencies may stem from the experimental conditions performed in Lin's work [12]. The installation of an exhaust jacket around the lower injection nozzle may yield an external, unsymmetric (with respect to the stagnant plane) pressure gradient distribution in the present OJF problems. As a result, the entrainment and outlet boundary conditions are not exactly as those specified in Section 2.

The comparison of the two similarity (inviscid and viscous) solutions, the numerical solution and the experimental data of radial velocity distribution at the section of $r^* = 11$ mm for the non-identical OJF is presented in Fig. 4. Apparently, the position of the stagnant plane is shifted towards the nozzle with the smaller injection inertia, i.e. the He jet. As a result of the immiscible assumption, both inviscid and viscous solutions have sharp discontinuities at the stagnant position ($x_s = 0.74$) which are not found in the numerical and experimental investigations. This reveals that the mixing of He and air jets in the regions near the stagnant plane is significant and cannot be ignored. It is noted that the differences between the inviscid and viscous solutions in the He (upper) side are larger than in the air (lower) side as indicated in Fig. 4. This is attributed to the smaller initial Reynolds number ($Re = 84$) in the He jet than $Re = 660$ in the air jet. As Re decreases, the viscous term appearing in equation (10) becomes more important and, thus, cannot be dropped in the problem formulation. On the other hand, the numerical solution which takes into account all transport processes gives a very satisfactory result as compared with the experimental data. Note that the relatively significant discrepancies between the numerical and experimental results also appear in the region around $x/L = 0.5$ as we have observed in Fig. 3. In order to support explicitly the foregoing argument that the mixing process is important in the fomulation of non-identical OJF, the axial

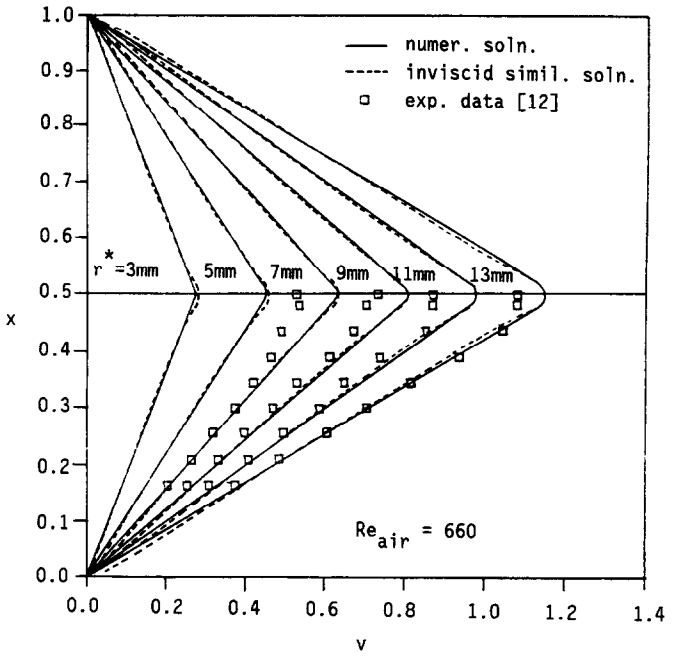

FIG. 3. Comparisons of numerical and similarity solutions of radial velocity with experimental data for identical OJF without rigid-body rotation at six radial sections.

distributions of species mass fraction at the axis of symmetry are plotted in Fig. 5. It is clear that the two fluids (He and air) are not immiscible and the thickness of the mixing layer is about one fifth of the separation distance between the two nozzles in this case.

4.2. *Identical OJF with rigid-body rotation*

In this case, air is introduced into both the upper and lower injection nozzles which rotate in opposite directions, i.e. $-w_1^0 = w_2^0$, with $-u_1^0 = u_2^0 = 0.453$ m s^{-1}. The axial and circumferential velocities vanish at the stagnation plane ($x_s = 0.5$) and have different

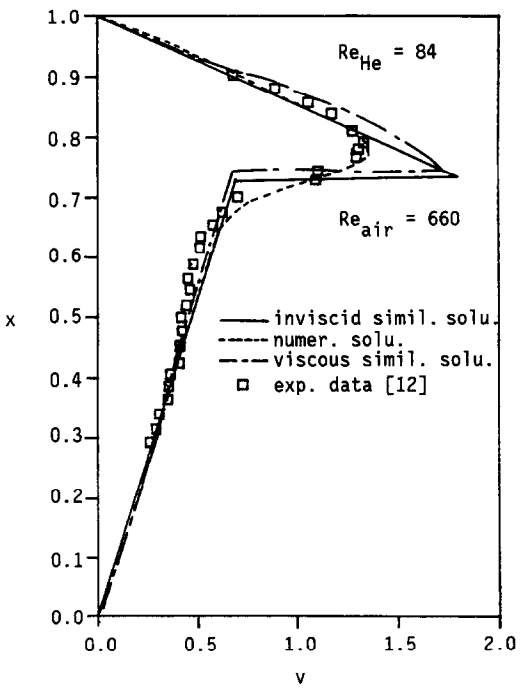

FIG. 4. Comparisons of numerical and similarity solutions of radial velocity with experimental data for non-identical OJF without rigid-body rotation at radial section of $r^* = 11$ mm.

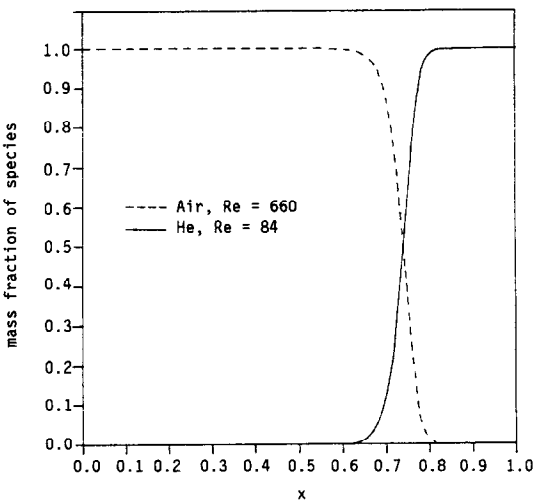

FIG. 5. Profiles of mass fractions of He and air for non-identical OJF without rigid-body rotation at axis of symmetry.

signs in the upper and lower half parts of the flow field. Basically, the centrifugal force (w^2/r) and the inertia force ($v\partial u/\partial x$) are balanced by the radial pressure gradient, according to equation (20), near the injection planes of the nozzles. The radial pressure gradient remains almost the same but u and w vanish as the fluid approaches the stagnant plane along the axial direction. This radial pressure gradient directed inwardly to the axis of the jets weakens the radially outward flow in the regions near the stagnant plane. Increasing the magnitude of $\partial p/\partial r$ will eventually induce a radially inward secondary flow resulting in the formation of a recirculation zone on either side of the stagnant plane, as depicted in Fig. 6(b), which is well known as the 'tea cup' effect [22]. The value of $\partial p/\partial r$ is proportional to the second power of the rotation speed, ω, based on the expression of equation (A12). Figure 6 shows schematically the evolution of the recirculation zone which has been experimentally observed by Lin [12] using the flow visualization technique. When the rotation speed is increased, the region of recirculation with ordered streamlines grows in size both axially and radially. As the outside boundary of the flow field is under atmosphere conditions, the thickness of the recirculation zone remains constant in the central portion of the OJF but is reduced by diminishing the pressure gradient in large radial distance as illustrated in Fig. 6(b). Due to the rotation speed being increased further, the well defined laminar recirculation zone breaks down and small unsteady eddies are generated within the recirculation zone, as illustrated in Fig. 6(c). This means that the type of OJF has moved from the laminar regime to the transition regime.

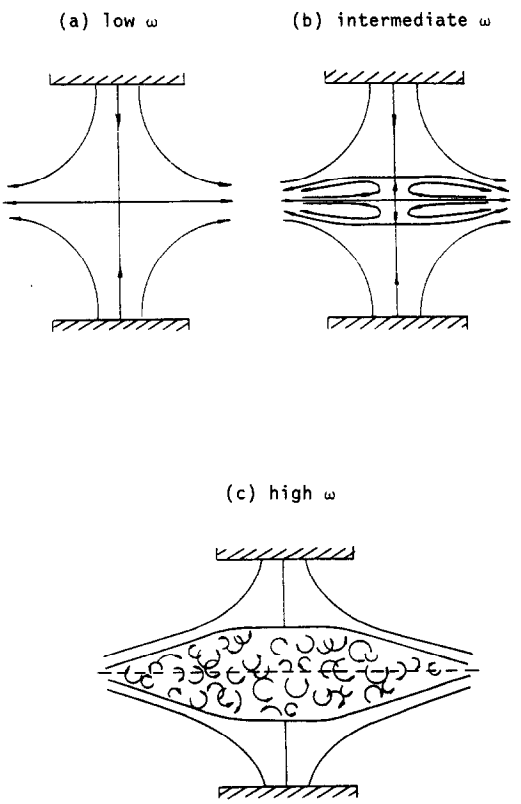

FIG. 6. Schematics of evolution of recirculation zone in identical OJF with rigid-body rotation.

Figure 7 compares the numerical predictions of the axial distributions of the radial velocity with the experimental data at the radial section of $r^* = 14$ mm for six different rotation speeds. It can be seen from Fig. 7(b) that the negative radial velocities appear in the regions near the stagnant plane when the rotation speeds exceed 10 rev s^{-1}. This shows the formation of recirculation zones around the stagnant plane. The agreements of the numerical solutions and experimental data presented in Fig. 7 are generally good except for the case with $\omega = 12$ rev s^{-1}. Lin [12] observed from the experiment that numerous small unsteady eddies start to form inside the recirculation zone, as illustrated in Fig. 6(c), when the rotation speed slightly exceeds 12 rev s^{-1} with the present case of $Re = 660$. It is, therefore, speculated that the case with $\omega = 12$ rev s^{-1} may lie in the ambiguous border between the laminar and transition regimes. Accordingly, the solution of the present laminar formulation for the case with $\omega = 12$ rev s^{-1} cannot agree well with the experimental data.

The influence of the viscous–vorticity interaction term, which appeared in equation (A10), is found to be small in the present case incorporated with a small ratio of Rossby number to Reynolds number ($Ro/Re < 10^{-2}$). Only the inviscid similarity solutions are presented in the following discussion. Both similarity and numerical solutions of the radial velocity distribution at the radial section of $r^* = 14$ mm are displayed in Fig. 8. The comparison shows that, as the rotation speed is increased, the discrepancy between these two solutions becomes more significant. The comparisons of the similarity and numerical solutions with the experimental data for the axial distributions of axial velocity and the radial distributions of circumferential velocity are presented in Figs. 9 and 10, respectively. In general, the discrepancies between the numerical and similarity solutions have the same trends as shown in Fig. 8. A comparison from Fig. 10 reveals that the discrepancy becomes larger as the radial position moves far away from the central part of the rotating porous disks. This is primarily attributed to the assumption of an infinite-diameter disk embedded in the similarity solution. It is also observed from Fig. 10 that the numerical and experimental results have different trends as the radial position moves closer to the rim of the disk particularly with large rotation speeds. This may be attributed to the existence of an external pressure gradient field stemming from the exhaust system in Lin's experiment [12]. In general, both theoretical solutions have fair agreements with the measurements, but the error of

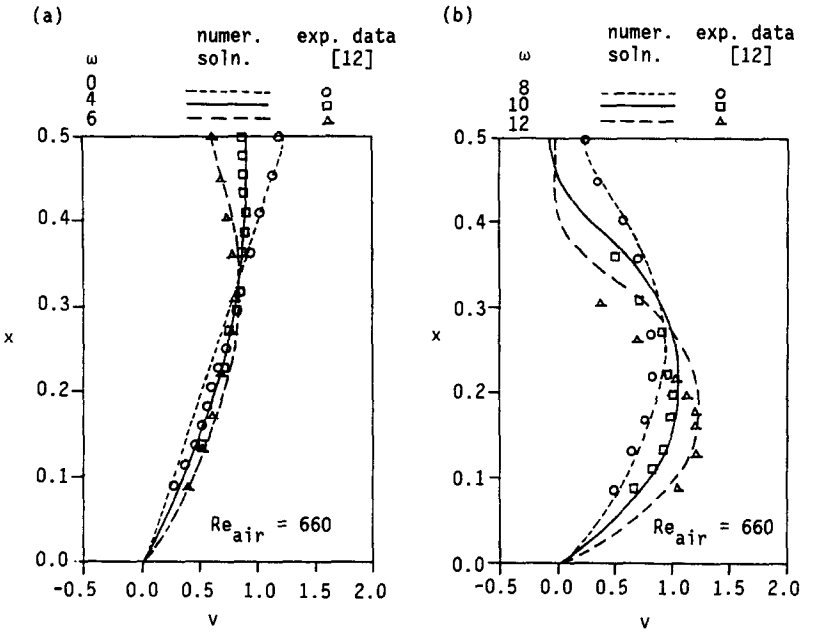

FIG. 7. Comparisons of numerical solutions of radial velocity with experimental data for identical OJF with six different rotation speeds at radial section of $r^* = 14$ mm.

the similarity solution grows with increasing rotation speed.

5. CONCLUSIONS

Numerical analysis of the finite, laminar OJFs are performed and compared with the analytical solutions and the measurements made by Lin [12]. It shows that the corresponding transport equations associated with the finite-volume method employed in this work can yield accurate predictions of the OJF problems. Analytical solutions are all obtained from the self-similar equations with some approximations and, accordingly, have some limitations in practical applications. First, the assumption of the infinite diameter of the disks restricts the similarity solutions being applicable to the central part of the interest domain only. Secondly, the error of similarity solution grows generally with the increasing rotation speed. In addition, the exclusion of mixing process in the formulation of the non-identical OJF constituted by two

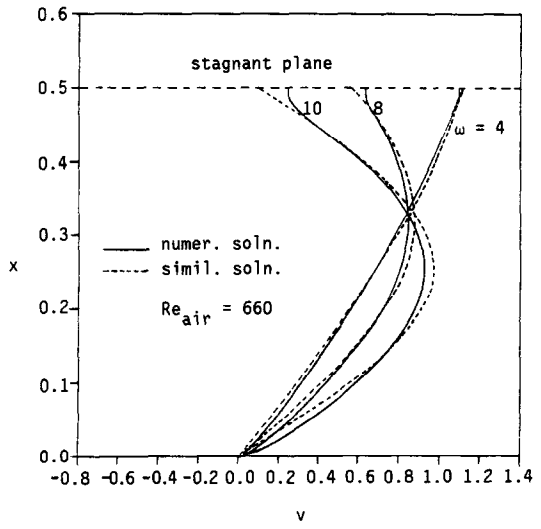

FIG. 8. Comparisons of numerical and similarity solutions of radial velocity for identical OJF with three rotation speeds at radial section of $r^* = 14$ mm.

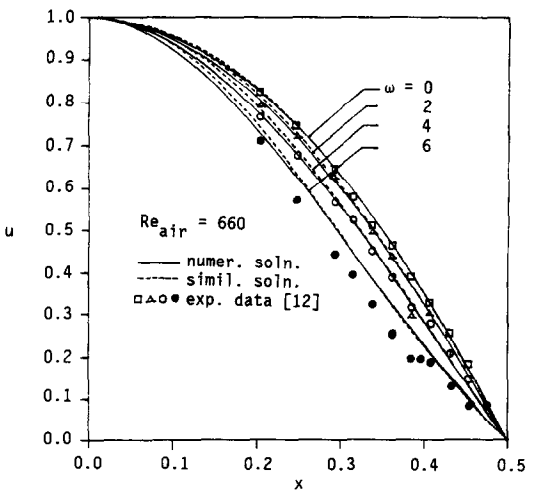

FIG. 9. Comparisons of numerical and similarity solutions of axial velocity with experimental data for identical OJF with four rotation speeds at radial section of $r^* = 14$ mm.

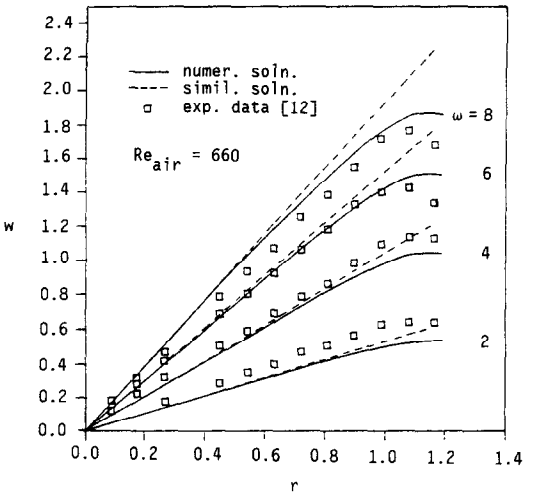

FIG. 10. Comparisons of numerical and similarity solutions of circumferential velocity with experimental data for identical OJF with four rotation speeds at axial section of x^* = 4 mm.

different fluids fails in the flow field prediction in the mixing layer. Nevertheless, the simple forms of the self-similar equations permit us to qualitatively investigate the OJF problems with less effort in the preliminary stage. It is also found that the viscous effects in the present OJF problems are small and the inviscid, closed-form solutions can give fair predictions in the study.

REFERENCES

1. Z. H. Chen, G. E. Liu and S. H. Sohrab, Premixed flames in counterflow jets under rigid-body rotation, *Combust. Sci. Technol.* **51,** 39–50 (1987).
2. G. I. Sivashinsky and S. H. Sohrab, The influence of rotation on premixed flames in stagnation-point flow. *Combust. Sci. Technol.* **53,** 67–74 (1987).
3. T. H. Lin and S. H. Sohrab, Influence of vorticity on counterflow diffusion flames, *Combust. Sci. Technol.* **52,** 75–90 (1987).
4. T. H. Lin and S. H. Sohrab, Diffusion flames in opposed counter-rotating jets, *Combust. Sci. Technol.* **63,** 193–207 (1989).
5. W. J. Sheu and S. H. Sohrab, Extinction of counterflow diffusion flames in counter-rotating finite jets, *Combust. Sci. Technol.* **60,** 39–57 (1989).
6. T. H. Lin and S. H. Sohrab, On the transition of diffusion to premixed flames in conserved systems, *Combust. Flame* **68,** 73–79 (1987).
7. G. K. Batchelor, Note on a class of solutions of the Navier–Stokes equation representing steady rotationally-symmetric flow, *Q. J. Mech. Appl. Math.* **4,** 29–41 (1951).
8. I. Proudman, An example of steady laminar flow at large Reynolds number, *J. Fluid Mech.* **9,** 593–602 (1960).
9. K. Seshadri and F. A. Williams, Laminar flows between parallel plates with injection of a reactant at high Reynolds number, *Int. J. Heat Mass Transfer* **21,** 251–253 (1978).
10. C. Y. Wang, Impinging stagnation flow, *Physics Fluids* **30,** 915–917 (1987).
11. J. D. Goddard, J. B. Melville and K. Zhang, Similarity solutions for stratified rotating-disk flow, *J. Fluids Mech.* **182,** 427–446 (1987).
12. T. H. Lin, Studies on homogeneous and heterogeneous reactive flows, Ph.D. thesis, Northwestern University (1987); also in T. H. Lin and S. H. Sohrab, Finite jets with and without rigid-body rotation, Fall Technical Meeting of the Combustion Institute, San Juan, Puerto Rico (December 1986).
13. R. K. Agarwal and W. W. Bower, Navier–Stokes computations of turbulent compressible two-dimensional impinging jet flowfields, *AIAA J.* **20,** 577–584 (1982).
14. C. J. Hwang and J. L. Liu, Numerical study of two-dimensional impinging jet flowfields, *AIAA J.* **27,** 841–842 (1989).
15. C. Prakash, U. S. Powle and N. V. Suryanarayana, Analysis of laminar flow and heat transfer between a stationary and a rotating disk, *AIAA J.* **23,** 1666–1667 (1985).
16. P. G. Huang and J. M. MacInnes, Modeling the outwash flow arising from two colliding turbulent jets, 1st National Fluid Dynamics Congress, Cincinnati, Ohio (1988).
17. J. W. Buddenberg and C. R. Wilke, Calculation of gas mixture viscosities, *Ind. Engng Chem.* **41,** 1345–1347 (1949).
18. J. C. Slattery and R. B. Bird, Calculation of the diffusion coefficient of dilute gases and the self-diffusion coefficient of dense gases, *A.I.Ch.E. Jl* **4,** 137–142 (1958).
19. S. V. Patankar, *Numerical Heat Transfer and Fluid Flow*. McGraw-Hill, New York (1980).
20. J. F. Thompson, W. U. A. Warsi and C. W. Mastin, *Numerical Grid Generation*. North-Holland, Amsterdam, The Netherlands (1985).
21. T. von Kármán, Über laminare und turbulent Reiburg, *AZMM* **1,** 233–235 (1921).
22. H. Schlichting, *Boundary Layer Theory*, 7th Edn, p. 214. McGraw-Hill, New York (1979).

APPENDIX

A.1. Non-identical OJF without rigid-body rotation

On the basis of specified governing equations (8)–(10) we define a stream function Ψ_i as

$$\Psi_i = -r^2 f_i(x) \tag{A1}$$

and result in the expressions of the velocity component as

$$u_i(r,x) = \frac{1}{r}\frac{\partial \psi_i}{\partial r} = -2f_i(x) \tag{A2}$$

$$v_i(r,x) = -\frac{1}{r}\frac{\partial \psi_i}{\partial x} = rf_i'(x) \tag{A3}$$

where the superscript "′" denotes the differentiation with respect to x. Inserting equations (A2) and (A3) into equations (9) and (10), reduces these two momentum equations to a nonlinear ordinary differential equation

$$(f_i')^2 - 2f_i f_i'' - f_i'''/Re_i = A_1 \tag{A4}$$

where A_1 is an integration constant. The boundary conditions of equation (11) become $f_1(1) = -f_2(0) = 1/2$ and $f_1'(1) = f_2'(0) = f_i(x_s) = f_i''(x_s) = 0$.

Equation (A4) can be further simplified by dropping the viscous term under the limit of large Reynolds number and becomes

$$(f')^2 - 2f'f'' = A_1. \tag{A4'}$$

Note that

$$\left[\frac{(f')^2}{f}\right]' = \frac{f'[2ff'' - (f')^2]}{f^2}.$$

Substitution of equation (A4′) into the above equation and integration with respect to x yields

$$\frac{(f')^2}{f} = \frac{A_1}{f} + A_2$$

or

$$f' = \pm\sqrt{(A_2 f + A_1)} \tag{A5}$$

where A_2 is the second integration constant. Integrating equation (A5) once more, one obtains

$$\frac{2}{A_2}\sqrt{(A_2 f + A_1)} = \pm x + A_3$$

or

$$f = K_2 x^2 + K_1 x + K_0 \tag{A6}$$

where K_0, K_1 and K_2 are three constants. Employment of the boundary conditions in the upper part of the flow field gives

$$K_0 = \frac{1}{2} - \frac{1}{2(1-x_s)^2}, \quad K_1 = \frac{1}{(1-x_s)^2}$$

and

$$K_2 = -\frac{1}{2(1-x_s)^2}.$$

Based upon the definitions shown in equations (A2) and (A3), one obtains the inviscid solutions as expressed in equations (12)–(15).

A.2. Identical OJF with rigid-body rotation

Following the study of von Kármán [21], we assume that the velocity components have the form

$$u = F(z), \quad v = r\,Ro\,G(z), \quad w = r\,Ro\,H(z) \tag{A7}$$

where a new axial coordinate z is defined by

$$z = x\,Ro. \tag{A8}$$

Introduction of equations (A7) and (A8) into equations (18)–(21) leads to a reduced system of ordinary differential equations as follows:

$$F' + 2G = 0 \tag{A9}$$

$$G^2 - H^2 + FG' + \frac{Ro}{Re}G'' = B \tag{A10}$$

$$2GH + FH' - \frac{Ro}{Re}H'' = 0 \tag{A11}$$

where B is constant. From equation (20), the radial pressure gradient may also be expressed in the form of

$$\frac{\partial p}{\partial r} = -B\,Ro^2 r. \tag{A12}$$

The boundary conditions to be imposed on the solutions of equations (A9)–(A11) are

$$F(0) = 1, \quad G(0) = 0, \quad H(0) = 1 \tag{A13a}$$

$$G'(z_s) = 0 \quad \text{and} \quad H(z_s) = 0 \tag{A13b}$$

where $z_s = Ro/2$ denotes the position of the stagnant plane. As observed from equations (A10) and (A11), the viscous effect is coupled with the flow vorticity. However, the pure vorticity effect can be firstly studied from the above self-similar equations by dropping the viscous–vorticity interaction terms in equations (A10) and (A11). The inviscid solutions incorporated with the boundary conditions in equation (A13) have been given by [2, 12]

$$G(z) = \frac{\sin 2z}{1-\cos Ro} \tag{A14}$$

$$F(z) = H(z) = \frac{\cos 2z - \cos Ro}{1-\cos Ro}. \tag{A15}$$

Substitution of equations (A14) and (A15) into equation (A7) yields the inviscid solutions as expressed in equations (24)–(26).

ANALYSE DE JETS OPPOSES LAMINAIRES FINIS AVEC OU SANS ROTATION D'ENSEMBLE

Résumé—On étudie par voie théorique les mécanismes de mécanique des fluides et de mélange permanents, laminaires des jets opposés. Une méthode de volumes finis est employée pour résoudre numériquement les équations correspondantes de transport. Des résultats du calcul sont comparés avec les solutions analytiques affines et avec les données expérimentales pour deux cas de jets opposés non identiques, constitués par deux fluides différents sans rotation et de jets opposés identiques avec rotation. Les solutions numériques fournissent des prédictions précises tandis que les solutions affines donnent de bonnes prédictions sous certaines conditions.

ANALYSE VON BEGRENZTEN LAMINARSTRAHLEN IM GEGENSTROM MIT UND OHNE FESTKÖRPERROTATION

Zusammenfassung—Es wird die Fluidmechanik und der Mischungsprozeß von stationären laminaren begrenzten und sich im Gegenstrom bewegenden Strahlen theoretisch untersucht. Dazu wird eine Finite-Volumen-Methode verwendet, um die korespondierenden Transportgleichungen zu lösen. Die berechneten Ergebnisse werden mit den analytischen Ähnlichkeitslösungen und den experimentellen Daten für zwei verschiedene Fälle von Gegenstromstrahlen verglichen. Dabei handelt es sich um zwei unterschiedliche Fluide ohne Festkörperrotation sowie gleiche Gegenstromstrahlen mit Festkörperrotation. Die Übereinstimmungen zeigen, daß die von den kompletten Transportgleichungen erhaltenen numerischen Lösungen genaue Voraussagen liefern, während die Ähnlichkeitslösungen gute Voraussagen unter bestimmten Einschränkungen ergeben.

АНАЛИЗ ОГРАНИЧЕННЫХ ЛАМИНАРНЫХ ВСТРЕЧНЫХ СТРУЙ ПРИ НАЛИЧИИ И ОТСУТСТВИИ ИХ ВРАЩЕНИЯ КАК ТВЕРДОГО ТЕЛА

Аннотация—Теоретически исследуются механика и процесс смешения устойчивых ламинарных ограниченных встречных струй. Для численного решения соответствующих уравнений переноса используется метод конечных объемов. Результаты расчетов сравниваются с аналитическими автомодельными решениями и экспериментальными данными для двух случаев со встречными струями двух различных жидкостей при отсутствии вращения как твердого тела и с одинаковыми встречными струями при наличии такого вращения. Показано, что результаты численных решений полных уравнений переноса являются точными, в то время как автомодельные решения дают довольно точные результаты при некоторых ограничениях.